

RESEARCH ARTICLE | FEBRUARY 10 2021

The role of standing wave in the generation of hot electrons by femtosecond laser beams incident on dense ionized target

R. Babjak   ; J. Psikal 



Physics of Plasmas 28, 023107 (2021)

<https://doi.org/10.1063/5.0031555>



View
Online



Export
Citation

CrossMark

Articles You May Be Interested In

Effect of preplasma on energetic electron and ion generation by irradiation of ultra-intense laser pulses

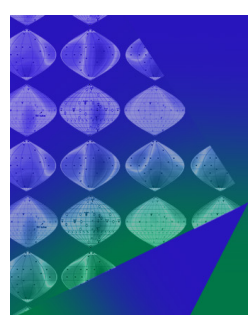
AIP Conference Proceedings (June 2008)

Preplasma effects on laser ion generation from thin foil targets

Physics of Plasmas (January 2020)

Electron acceleration by intense short laser pulse in the preplasma of a target

Physics of Plasmas (August 2009)



Physics of Plasmas
Features in Plasma Physics Webinars

Register Today!

 **AIP
Publishing**

The role of standing wave in the generation of hot electrons by femtosecond laser beams incident on dense ionized target

Cite as: Phys. Plasmas **28**, 023107 (2021); doi: [10.1063/5.0031555](https://doi.org/10.1063/5.0031555)

Submitted: 1 October 2020 · Accepted: 20 January 2021 ·

Published Online: 10 February 2021



View Online



Export Citation



CrossMark

R. Babjak^{1,2,a)} and J. Psikal¹

AFFILIATIONS

¹Faculty of Nuclear Sciences and Physical Engineering, Czech Technical University in Prague, Brehova 7, 115 19 Prague 1, Czechia

²Institute of Plasma Physics, Czech Academy of Sciences, Za Slovankou 1782/3, 182 00 Praha 8, Czechia

^{a)}Author to whom correspondence should be addressed: babjak@ipp.cas.cz

ABSTRACT

We demonstrate the differences in hot electron absorption mechanisms dominant in the interaction of a femtosecond laser pulse with intensities of 10^{18} W/cm² and 10^{21} W/cm² on a fully ionized target with a steep density profile and preplasma with moderate scale length ($3\ \mu\text{m}$). We show that acceleration of each electron starts at the moment when the magnetic component of a standing electromagnetic wave changes its polarity in a regime without preplasma. In the presence of preplasma, the stochastic heating is the dominant absorption mechanism along with the longitudinal electric field. It is observed that wave's energy is absorbed only if the standing wave is already created at the position of electron during the interaction with the pulse with an intensity of 10^{18} W/cm². In the case with 10^{21} W/cm² intensity, the part of the electrons is pre-accelerated in front of the target before the reflection and following stochastic heating. The presence of preplasma results in electron temperatures close to or even exceeding ponderomotive scaling. At higher intensity, the re-injection of electrons previously repelled by incident wave's ponderomotive force into high-field regions is allowed if the standing wave is created.

Published under license by AIP Publishing. <https://doi.org/10.1063/5.0031555>

28 August 2023 08:54:17

I. INTRODUCTION

The interaction of laser pulses with intensities exceeding 10^{18} W/cm² with overdense thin ionized targets has found many applications in recent years, e.g., laser-driven particle acceleration,¹ high harmonics generation,² fast ignition in inertial confinement fusion,³ or laboratory astrophysics.⁴ When an electromagnetic (EM) field at such intensities interacts with the plasma, a fraction of the radiation is absorbed via non-linear processes present during the interaction and the rest is reflected from the overcritical electron-plasma boundary (EPB). Therefore, the understanding of underlying radiation-matter coupling mechanisms is essential for this research.

Energy from the EM field that is absorbed is mostly converted into the population of electrons that are accelerated/generated near the target surface or in the underdense preplasma formed in front of the target. They are known as hot electrons. Many theoretical and empirical models have been proposed to explain such acceleration,^{5–11} but they differ in the prediction of electron properties such as the number of accelerated particles, quasi-temperature, cutoff energy, or angular distribution depending on the simulation/experimental parameters.

The acceleration mechanisms of hot electrons seem to be the most sensitive to laser intensity, preplasma profile, and angle of incidence of laser pulse on the target.

When the steep density profile is present, the acceleration is strongly influenced by the quasi-static electric field created at the EPB^{12,13} and by the electromagnetic field in the form of the standing wave created due to the interference of incident and reflected laser pulse.^{14–16} When preplasma^{17,18} is present, the coupling is explained mostly by stochastic heating^{19–22} or direct laser acceleration (DLA) mechanism.^{23,24}

This work aims to provide further insight into the regime of interaction when the femtosecond laser pulse is incident normally on the target. In the case of steep plasma density profile, we discuss in detail the ejection of electrons into the vacuum caused by the electrostatic field created at the vicinity of EPB and their acceleration in the standing wave created in front of the target. When the intensity of the incident laser pulse is higher, we demonstrate the effect of target surface deformation due to strong ponderomotive pressure. In preplasma, the hot electron acceleration mechanism strongly differs compared to the acceleration in the vicinity of EPB at the sharp interface and leads

to electron temperatures close to or even exceeding ponderomotive scaling. We clearly demonstrate the necessity for the standing wave in order to accelerate electrons in moderate length preplasma (in order of μm) and the presence of stochastic heating and describe why longer preplasma results in higher electron energies. For higher intensity, we show that in the presence of the standing wave, electrons previously repelled by the ponderomotive force can be re-injected into the high-field regions. We also propose an explanation for the higher temperatures of hot electrons in the case of p-polarization compared to s-polarization in the target with preplasma.

II. METHODS AND SIMULATIONS PARAMETERS

In order to study hot electron generation, the 2D version of particle-in-cell (PIC) code Smilei²⁵ was used. A linearly p-polarized laser pulse with $\lambda = 800 \text{ nm}$ and intensities of 10^{18} W/cm^2 and 10^{21} W/cm^2 at maximum (i.e., with dimensionless pulse amplitudes $a_0 \approx 0.68$ and $a_0 \approx 21.6$, respectively) was incident on a target with a sharp density profile and on the target with preplasma in front of the dense thin foil. The combination of density profiles and pulse intensities resulted in four investigated scenarios. For simplicity, plasma containing only electrons and protons was used. The density of overdense foil was $\approx 30 n_c$ (which corresponds to fully ionized hydrogen in the density of solid state), where n_c is critical density. Scale length of exponentially increasing density of preplasma $n = n_c \times \exp(x/L)$ for $-14.5 \mu\text{m} < x \leq 0 \mu\text{m}$ was $L = 3 \mu\text{m}$, until the overdense part of the target with constant maximum density located at $0 \mu\text{m} < x < 5 \mu\text{m}$ was reached. The target with a steep density gradient contained only overdense thin foil and the above defined preplasma was put in front of the target for the other studied case. The size of the grid cell was set to $16 \text{ nm} \times 16 \text{ nm}$, 50 macroparticles per cell were used for the overdense part and preplasma contained 16 macroparticles per cell due to its lower density. Laser pulse propagated toward the target in the x direction from the boundary located at x_{min} ($x_{min} = -12 \mu\text{m}$ for the target without preplasma and $x_{min} = -15 \mu\text{m}$ for the target with preplasma) with the beam axis at the position $y = 0 \mu\text{m}$, it had a trapezoidal temporal profile with a linear 10 fs intensity growth, 40 fs constant intensity, and 10 fs linear intensity decrease. The spatial profile was Gaussian, laser beam diameter (FWHM) was set to $4 \mu\text{m}$ at focus. The laser was focused into plane coordinates (0,0). The simulation box size was set to $31 \times 31\lambda^2$ and to $34 \times 31\lambda^2$ for targets without/with preplasma, which means that it contains 1488×1488 and 1632×1488 cells, 4.4×10^7 and 7.8×10^7 macroparticles, respectively. The initial temperature of the macroparticles was 1 keV, the macroparticles were frozen before (pre-)plasma interaction with the laser in the simulations. The cell size was set to be about 2/3 of the skin depth in order to resolve the relevant physics. Units in the figures are either specified explicitly, or following reference values are used for the normalization: electric field $E_r = m_e c \omega / e$, magnetic field $B_r = m_e \omega / e$, momentum $p_r = m_e c \omega$, and force $F_r = m_e c \omega$, where m_e is the mass of an electron, c is the speed of light, ω is the laser frequency, and e is the elementary charge.

This work makes frequent use of particle tracking diagnostics implemented in Smilei together with test particles. Test particles do not contribute to charge and current densities, but the code calculates their trajectories from EM fields at their location. We saved position, momenta, and fields at the position of tracked particles. At simulations with the steep density profile, test electrons were put at the

vacuum-plasma interface into the strip of width 3λ ($x = \langle 0, 3\lambda \rangle$) irradiated by the laser beam where hot electrons are expected to be generated. For simulations with preplasma, test electrons are present along the entire length of preplasma in the x direction. In the y direction, test electrons were placed inside the region $y = \langle -6\lambda, 6\lambda \rangle$ both in simulation with and without preplasma. Their location is displayed in yellow in Fig. 1. All particles were tracked from the beginning of the simulation.

Hot electron population can be easily distinguished from the target bulk electron population in energy distribution function. Hot and cold electron temperatures can be assigned to both populations with Boltzmann energy distribution.^{26,27} Therefore, the minimal energy E_{min} of hot electron population can be defined at the place where the slope of high energy tail changes in energy distribution function. During the post-processing, only those particles that were inside the overdense part of the target while satisfying the condition $E > E_{min}$ were analyzed.

III. STEEP DENSITY GRADIENT

When the laser pulse interacted with the target with the steep density gradient, the interaction started at time $17.5T$ and finished at time $40T$, where T is the laser period.

A. Intensity 10^{18} W/cm^2

The hot electron acceleration mechanism observed in our simulation results can be described as follows; in Fig. 2, the development of tracked electron quantities during the acceleration is depicted. This development of momentum and fields acting on the particle represents qualitative behavior common for all hot electrons. At the beginning of each acceleration process, the growth of momentum in a direction out of the target ($p_x < 0$) occurs. This happens due to the effect of an electrostatic field pulling the electron out to the vacuum as can be seen in Fig. 2(a) at a time around $31.5T$. p_x is negative at the same time when the E_x component of electric field is positive at the position of the particle, which results in the electric component of Lorentz force acting on the electron in a direction out of the target, see Fig. 2(b). The magnetic component of Lorentz force (B) has no impact on the electron being pulled out to the vacuum. The electrostatic field on the boundary of plasma and vacuum is created because of the oscillation

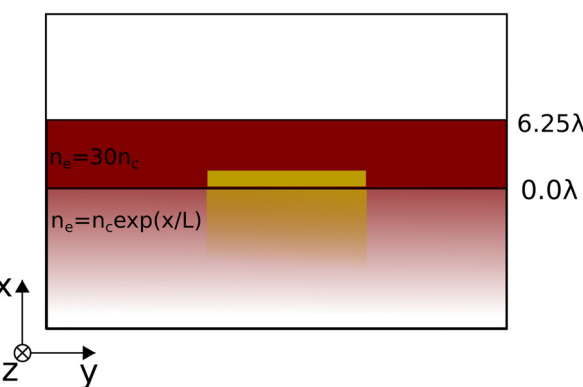


FIG. 1. The position of the overdense target with the preplasma in front of it. The position of test particles is shown in yellow.

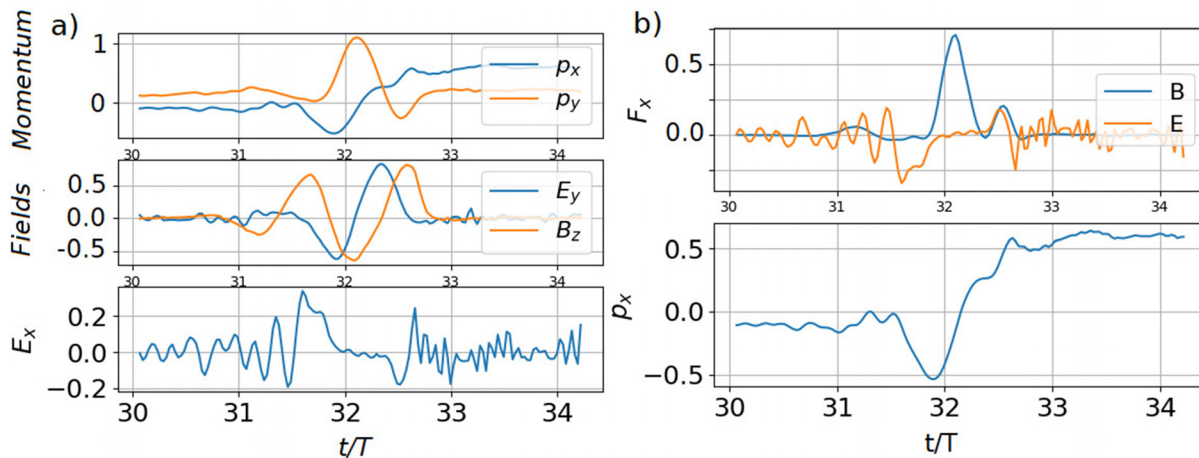


FIG. 2. (a) The development of momentum and fields acting on an electron during the acceleration process by a normally incident laser pulse with an intensity of 10^{18} W/cm^2 . (b) The time evolution of forces acting on the electron. At the beginning, the electrostatic force (E) pushes the electron to the area in front of the target and consequently the magnetic part of Lorentz force (B) causes the acceleration inside the target.

of electrons around immobile ions (on the timescale of a laser period as they have much larger mass) with a frequency of 2ω , where ω is the laser frequency. This ejection of electrons into the vacuum by an electrostatic field was previously described in Refs. 12 and 28.

When the electron is already in the vacuum, it interacts with the standing EM wave created in front of the target and depicted in Fig. 3. The electric component of the standing wave E_y causes electron to gain momentum in the direction along the target surface. Acceleration in the x -direction starts at the moment when the magnetic field perpendicular to the plane of incidence B_z changes its sign as shown in Fig. 2(a) in time shortly before $32T$. At that time, the product of $v_y B_z$ is negative, so the Lorentz force acts on a negatively charged electron in a positive direction toward the target. Relativistic values of velocity v_y lead to a relatively high strength in the magnetic part of Lorentz

force in the perpendicular direction to the standing wave's B_z and E_y fields orientation, i.e., perpendicular to the target surface. The process of acceleration ends at the moment when the particle crosses the plasma boundary and does not feel the standing wave field. The typical trajectories of accelerated electrons can be seen in Fig. 4(a).

According to how the acceleration process was described, it is possible to assume that the standing wave structure has the most significant impact on the acceleration process. Electrons immediately react to changes of the perpendicular electric field E_y . It is also possible to see that B_z and p_y values are shifted by π in phase and they have the same period. Thus, the force proportional to $v_y B_z$ is always positive. Since the electric field is harmonic in time, the phase shift between p_y and E_y is $\pi/2$. The phase shift between E_y and B_z , which is also $\pi/2$ (see Fig. 3), causes the previously mentioned π phase shift of p_y and B_z . The action of the magnetic part of Lorentz force thus twice a period accelerates electrons into the target.

All hot electrons were accelerated in the region between the first node of the magnetic field at distance $\approx 1/4\lambda$ in front of the target and EPB, see Fig. 3. In Fig. 5, points on the graph show the time and the position of electrons at the beginning of acceleration. The color gives information about the maximum longitudinal momentum of electrons after the acceleration. The beginning of the acceleration is defined as the moment when p_x reaches its minimal value. The acceleration twice a period typical for $\vec{j} \times \vec{B}$ heating can be observed from vertical bunches repeating every half-period. As mentioned before, acceleration starts at the moment when the magnetic field changes its sign. This happens at the same time at positions of all the electrons in front of the target twice a period. That is the reason why all electrons within one bunch start to be accelerated at the same time regardless of their position.

Note that the minimal x -position of each accelerated electron is slightly further from the target than the position depicted in Fig. 5(a) as the longitudinal momentum p_x is still negative at the beginning of the electron longitudinal acceleration toward the target. The minimum position of electrons during their longitudinal acceleration toward the target is about $x = -0.15\lambda$ which means that electrons still do not

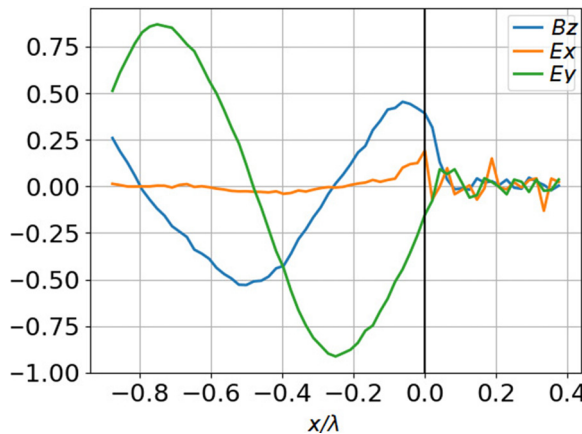


FIG. 3. Standing wave which was created after the reflection of the laser pulse with intensity 10^{18} W/cm^2 from the target without preplasma at time $33.4T$. Fields are normalized by reference fields: electric field $E_r = m_e c \omega / e$ and magnetic field $B_r = m_e \omega / e$. It may be seen that the standing wave is shifted because of finite conductivity of the target.

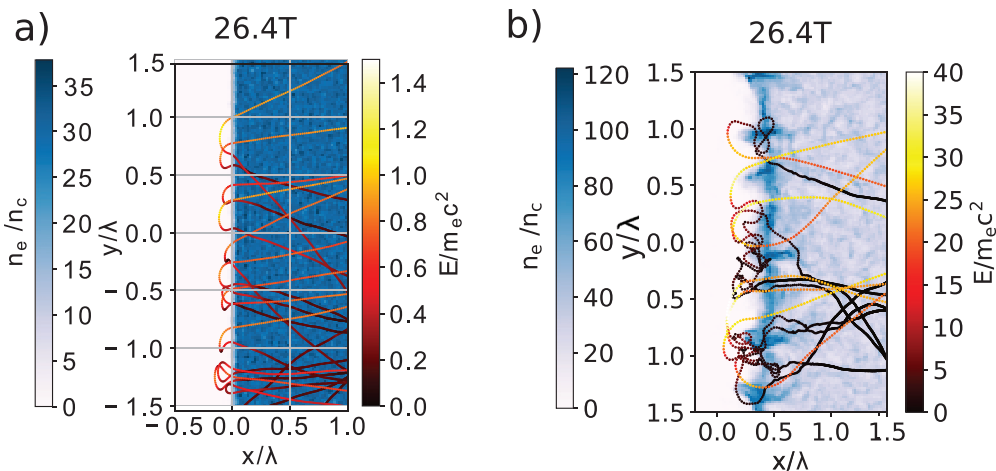


FIG. 4. Density of the target during the interaction with the laser pulse with intensity 10^{18} W/cm^2 (a) and 10^{21} W/cm^2 (b) with typical electron trajectories. It can be seen that EPB is completely unperturbed for lower intensity and electrons are accelerated immediately after being pulled out of the target. Higher intensity pushes the EPB inside the target and electrons oscillate chaotically before being accelerated.

move further than the magnetic field node at $x \approx -1/4\lambda$. One can expect that the position of an electron during the acceleration determines its longitudinal momentum increase after the acceleration which depends on the transverse electric field E_y , transverse magnetic field B_z , and electron acceleration time. The thickness of the acceleration region in front of the target should be proportional only to the strength of the longitudinal field E_x pulling electrons out into the vacuum. In the semi-analytical model¹² assuming infinite ion density gradient with immobile ions, the strength of such E_x field is theoretically fully determined by the laser pulse amplitude and the plasma density. However, the target expands during the interaction with the main laser pulse and due to non-zero temperature of plasma before the main pulse interaction (electron heating by laser pedestal or by picosecond slope of the pulse rising slowly compared to an ideal Gaussian pulse²⁹). Therefore, the width of the acceleration region strongly depends on the real value of steep ion density gradient and evolves during the interaction (increases with decreasing density

gradient in time). That is also apparent in Fig. 5(a) where more than 90% of the electrons start to be accelerated in the x -direction at the position $0 > x > -0.05\lambda$ at time around $24T$ but at wider region $0 > x > -0.1\lambda$ at later time around $32T$.

B. Intensity 10^{21} W/cm^2

When a laser pulse with an intensity of 10^{21} W/cm^2 was incident on the target with a steep gradient, the interaction regime significantly changed from the idealized scenario. The strong radiation pressure deformed the target and bored a hole in it. Consequently, the initially step-like interface was strongly disrupted and the interaction region consisted of local density, electric, and magnetic field disturbances. The curved shape of the overdense plasma boundary caused that the reflected wave was strongly non-uniform. Therefore, the standing wave in front of the target was far from ideal. Due to many violations in the interaction geometry, hot electrons were

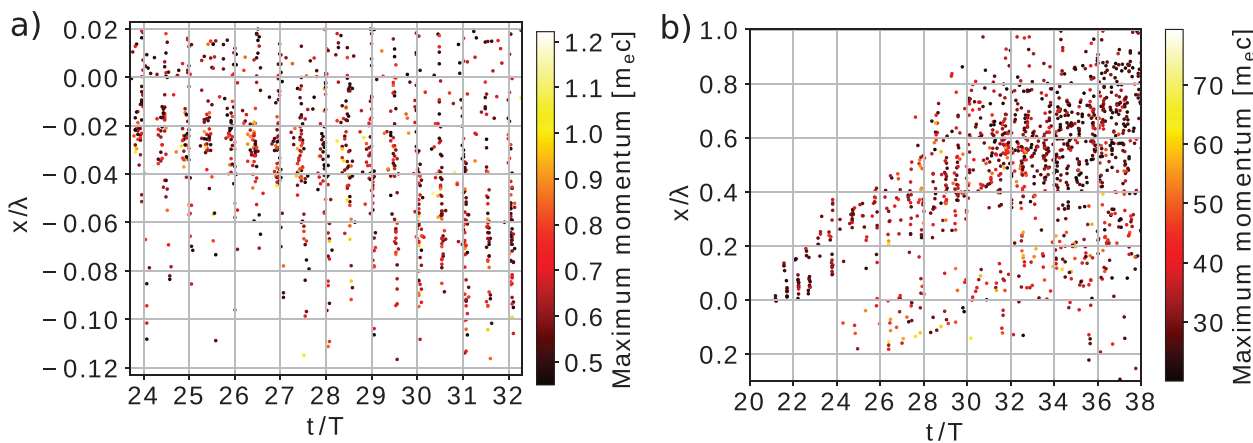


FIG. 5. Times and positions when electron acceleration toward the target started during the interaction with normally incident pulse of intensity (a) 10^{18} W/cm^2 and (b) 10^{21} W/cm^2 on the target with a steep density gradient.

accelerated and decelerated in front of the target before they crossed the boundary of the overdense foil, as can be seen in Fig. 4(b). The impact of electric field on the process of acceleration is negligible, and longitudinal motion of the electron is determined by the magnetic component of Lorentz force.

In Fig. 5(b), one can see the starting points of acceleration defined in the same manner as in the previous case. The pushing of EPB into the target can be observed in the left top corner. It can be estimated from the figure that the plasma layer was pushed with the velocity $\sim 0.08c$. The value of EPB velocity agrees with the value obtained from the density changes in time. Since the electrons are mostly accelerated close to the boundary, the starting point of acceleration moves with it. First, it moves quickly up to the moment when an equilibrium is established between the electrostatic pressure generated by the compressed electron cloud and the radiation pressure of the laser beam on the timescale of the laser period.³⁰ Then, the hole boring process continues both in electron and ion densities during the whole interaction.³¹ This can be seen in the figure up to the time around $31T$ when the points are more scattered along the x -position due to the increasing difference in EPB deformation along the y -axis.

The estimated EPB deformation at the first moment of the pressures equilibrium³⁰ $\Delta_{init} = \sqrt{4\epsilon_0 I/c/(en_e)} \approx 130 \text{ nm}$ and the estimated hole boring velocity³¹ $u_{hb}/c = \sqrt{\Xi}/(1 + \sqrt{\Xi}) \approx 0.06$, where $\Xi = I/(m_i n_i c^3)$, agrees well with our observations in the simulation. According to these analytical estimates, one can expect less pronounced deformation of the target by the strong radiation pressure with increasing target density (e.g., using metal foils). Note that the EPB deformation can be seen in Fig. 4(b) when the deformation exceeds the initial value Δ_{init} due to the hole boring process after the initial EPB deformation.

The width of the acceleration region is substantially larger along the x -direction compared with the 10^{18} W/cm^2 case. Although the standing wave structure is disrupted, it is apparent that some electrons are accelerated beyond the first node of the magnetic field in this non-ideal standing wave. Two strips of points where electrons are started to be accelerated are perceptible in Fig. 5(b). The strip located closer to EPB is between EPB and the first node, the other strip is at some distance from the first magnetic field node where the combination of

instantaneous transverse electric field E_y and magnetic field B_z is favorable for the electron acceleration toward the overdense plasma.

The initial density of overdense target $n_e \approx 30n_c$ is relatively low with regard to the commonly presented threshold for relativistic transparency $a_{th} = n_e/n_c$ which is close to the pulse amplitude $a_0 \approx 22$ for a given laser intensity. However, this threshold is essentially increased to $a_{th} \approx 0.65(n_e/n_c)^2$ for $(n_e/n_c) \gg 1$ in the case of non-uniform plasmas due to the action of the ponderomotive force which pushes the electrons into the plasma creating a strong peaking of the plasma electron density.³² Moreover, the total pulse length is 60 fs in our case, which is not enough for substantial plasma expansion and lowering the plasma density. Thus, we are still far from the relativistically induced transparency regime during the whole interaction even with the lowest solid density foil made from hydrogen.

IV. EFFECTS OF PREPLASMA

In the study of the interaction of laser pulse with the overdense target slightly evaporated by the pulse pedestal, a preplasma with exponentially increasing density $n_e = n_c \times \exp(x/L)$ for $x \leq 0$ and scale length $L = 3 \mu\text{m}$ was used in front of the overdense ionized foil located at $0 < x < 5 \mu\text{m}$, see Fig. 1. Therefore, the distance between the simulation box boundary where the laser pulse enters and the overdense plasma had to be increased and the laser pulse started to reflect from the overdense thin foil at the time $20T$ and stopped the interaction at the time $42.5T$.

A. Intensity 10^{18} W/cm^2

The presence of the preplasma in front of the target significantly changed the interaction regime. Most of the electrons were accelerated in the underdense preplasma, not in the proximity of the overdense plasma boundary like in the previous case with the steep gradient.

The acceleration process can be described as follows: while the laser pulse propagates through the preplasma, electrons oscillate perpendicularly to the pulse propagation direction due to the effect of the oscillating electric field. When the laser wave is reflected, it starts to propagate in the direction out of the target and the superposition of reflected and incident wave creates a non-ideal standing wave. At the

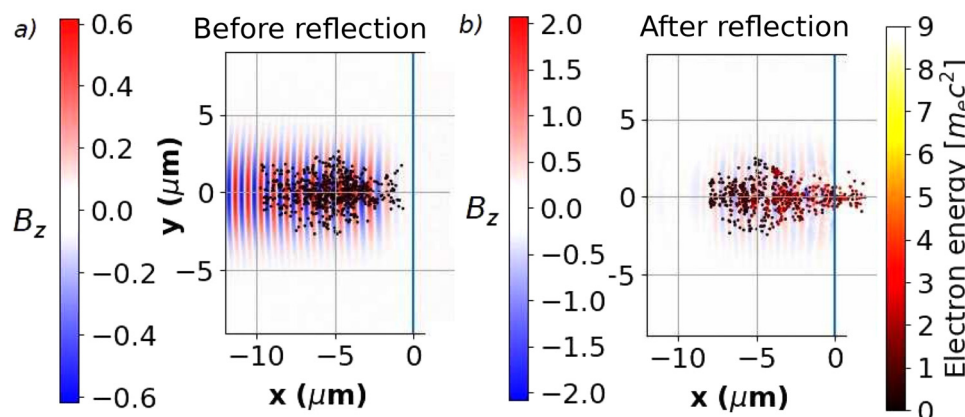


FIG. 6. (a) Electrons oscillating perpendicularly in the preplasma at the position of the laser pulse with the intensity of 10^{18} W/cm^2 propagating toward the overdense part of the target. (b) Electrons on the right from the reflected wave's wavefront at $x = -6 \mu\text{m}$ are red which means that they were already accelerated toward the overdense part of the target while those on the left are still oscillating in the field of the incident wave.

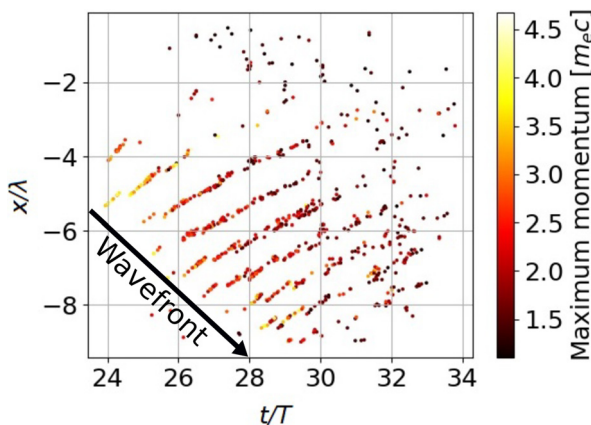


FIG. 7. Times and positions when electron acceleration toward the target started during the interaction with the pulse with the intensity of 10^{18} W/cm^2 on the target with preplasma. Black line shows the position of the reflected wave's front.

moment when the reflected wave reaches the position of the oscillating electron, it is accelerated inside the target as can be seen in Fig. 6. In Fig. 6(a), the electrons are not accelerated yet (black dots) because the laser pulse still propagates toward the overcritical target surface. In Fig. 6(b), the wavefront of reflected wave is located at around $x = -6 \mu\text{m}$ and the standing wave is already created at positions $x > -6 \mu\text{m}$. The color of electrons indicates that they are already accelerated into the target. It can be seen that the electrons on the left from the wavefront are not accelerated yet because the standing wave will be formed in that area when the reflected wave reaches this position later in time. This clearly shows the impact of standing wave on electron acceleration. The fact that electrons are not accelerated before the reflected wave reaches their position is demonstrated by the maximum distance of the acceleration from the target in Fig. 7. The maximum distance from the target of the acceleration initiation increases with time and corresponds to the position of reflected wave's front. The position of the reflected wave's front is approximately shown by the black line.

The evolution of electron momentum and Lorentz force components acting on it is depicted in Fig. 8. The blue vertical line defines the starting point of the acceleration used in Fig. 7. It can be seen in

Fig. 8(a) that the starting point of acceleration is only a rough estimate since more p_x minima are present close to the vertical line. However, it is sufficient for our analysis.

Many electrons were accelerated in a way similar to that shown in Fig. 8(a). The negative momentum gain is again present followed by the acceleration toward the target. While the electron propagated through preplasma it was periodically accelerated until it reached the overdense plasma at time approximately $37T$. The final momentum gain was the result of several pushes by the standing wave and longitudinal E_x field during the propagation toward the target. On the other hand, some electrons had very similar p_x evolution during the acceleration process as the electrons accelerated in the target with steep gradient, see Fig. 8(b). At time around $25T$, the electron gains momentum in the direction away from the target and right after it is accelerated toward the target. Here, the initial negative momentum gain occurs in preplasma and does not mean pulling the electron out of the overdense plasma layer. The second difference is that mostly the longitudinal electric field component was responsible for the acceleration, not the standing wave field. However, the most of electrons were accelerated by the combination of several strong electric field pushes similar to Fig. 8(b) and by the chaotic accelerations and decelerations similar to Fig. 8(a). Typical electron trajectories are depicted in Fig. 9.

To quantify the effect of mentioned acceleration mechanisms, the contribution of electric field components was expressed using the formula $\gamma^2(t) - \gamma_0^2 = -2 \int_{t_0}^t E_x p_x d\tau - 2 \int_{t_0}^t E_y p_y d\tau - 2 \int_{t_0}^t E_z p_z d\tau = I_x + I_y + I_z$, where γ_0 is the initial gamma factor of the accelerated electron. The value of integral I_x represents the contribution of longitudinal electric field to the acceleration which can be present because of the charge separation by the ponderomotive force and the laser self-focusing. The integral I_y represents the contribution of the background transverse field and the oscillating field of laser pulse which was consequently bend into the x -direction by the magnetic field. In a chosen geometry, the value of I_z can be neglected. The value of integrals was evaluated at the moment when the electron reached its maximum in p_x .

The effect of electric and magnetic field on the electron acceleration is comparable for electrons with lower maximal momentum, namely, $p_x^{\max} < 2.5 m_e c$, see Fig. 8(c). This is in agreement with the acceleration process described in Fig. 8(a), where the combination of electric and magnetic components of Lorentz force contributes to the

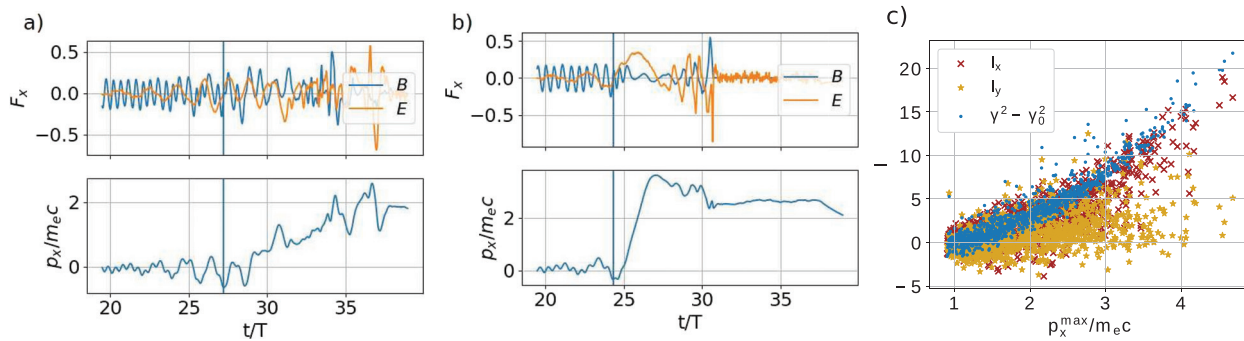


FIG. 8. The development of the Lorentz force components acting on the electron during the acceleration and longitudinal momentum p_x of the electron when the laser with the intensity of 10^{18} W/cm^2 is incident on the target with preplasma. Vertical line indicates the moment of acceleration initiation according to our definition. In (a), the electron was accelerated by the stochastic effect of electric and magnetic components of Lorentz force. In (b), the electron was accelerated by the longitudinal electric field. (c) The contribution of electric field components to the acceleration at the moment of p_x maximum and the increase in gamma factor.

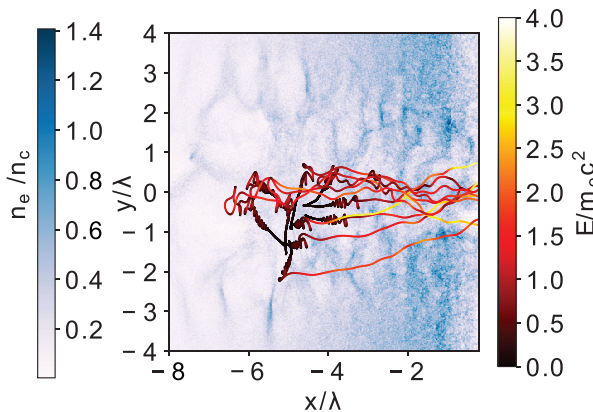


FIG. 9. Typical electron trajectories during the acceleration after the incidence of pulse with intensity 10^{18} W/cm^2 on the target with preplasma.

final momentum. Electrons with the highest energies were accelerated mostly by the longitudinal electric field, see Fig. 8(b).

The mechanism responsible for the acceleration by the transverse oscillating field is stochastic heating. The acceleration happens in the field of the standing wave and Lyapunov exponent³³ (also called Lyapunov coefficient) for accelerated electrons is positive. The value of Lyapunov exponent σ for two initially close trajectories in phase space with initial conditions \vec{x}_0 and $\vec{x}_0 + \Delta\vec{x}_0$ with the distance between two trajectories in phase space $d(\vec{x}_0, t) = ||\vec{\Delta x}(\vec{x}_0, t)||$ can be expressed as $\sigma = \lim_{d(\vec{x}_0, t_0) \rightarrow 0} \lim_{t \rightarrow \infty} (1/t) \ln [d(\vec{x}_0, t)/d(\vec{x}_0, t_0)]$, where $d(\vec{x}_0, t_0)$ is the initial distance in the phase space. We obtained the value of Lyapunov exponent from our PIC simulations in a following way. First, pairs of randomly selected hot electrons were created. The initial time t_0 was selected as a time when the reflected laser wave reached the position of the electron. Afterwards, the sequence of values $(1/(t_{end} - t_0)) * \ln [d(\vec{x}_0, t_{end})/d(\vec{x}_0, t_0)]$ for all the pairs was created as a function of the initial electron pair distance in the phase space $d(\vec{x}_0, t_0)$. The time t_{end} was chosen as a time when electrons were located in the overdense plasma so they did not interact with the field of the standing wave. The final value of Lyapunov exponent was obtained from the sequence as a limit for $d(\vec{x}_0, t_0) \rightarrow 0$.

The positive value of Lyapunov exponent demonstrates the stochasticity of electron motion. To confirm this, we performed the simulation with counter-propagating pulses with the intensity of 10^{18} W/cm^2 , where only test particles were present. The effect of the background field does not affect the electron motion in such simulation. The Lyapunov exponent of the electron motion in the standing wave created by the counter-propagating pulses was positive and the acceleration was present with maximum p_x exceeding m_ec . Only I_y was non-zero during this acceleration which means that electron's oscillations in the transverse direction were turned into positive x -direction. Based on this observation, we conclude that the mechanism responsible for the electron acceleration in PIC simulations is the combination of stochastic heating and the longitudinal electric field.

B. Intensity 10^{21} W/cm^2

Higher intensity of the laser pulse brought several new phenomena into the interaction compared to the case with the intensity of

10^{18} W/cm^2 , while the dominant impact of the standing EM wave was still present. Two hot electron populations can be distinguished in Fig. 10. The first one (population A) is located at x -axis position around $10 \mu\text{m}$ and another one is spread between $x = 0$ and $7 \mu\text{m}$ (population B). The rough estimate is that 45% of hot electrons belong to the population A and 55% belong to the population B. The population A does not seem to be formed of separate electron bunches as expected for the electrons accelerated by the normally incident pulse. The bunches were smoothed when the electrons crossed the rear side of the target at $x = 5 \mu\text{m}$ and were clearly visible at earlier times when they were still located in front of or inside the target. The distance between the bunches in the population B located inside the target is $\lambda/2$, identical as in the case of $j \times \vec{B}$ heating even though the electrons were not accelerated at the overdense plasma boundary but rather in preplasma.

The acceleration process can be described by Fig. 11. Four figures show the propagation of laser pulse in the preplasma toward the overdense plasma layer and hot electrons positions.

In Fig. 11(a), the laser pulse is propagating through the preplasma. The electrons are either pushed forward in front of the pulse or to the sides of the pulse by the ponderomotive force. The color of electrons shows that they were not accelerated yet because the laser pulse was still propagating toward the target and standing wave was not created yet.

In Fig. 11(b), the splitting of electrons into two populations can be already observed. The population A is located closest to the overdense layer marked by the blue vertical line. It is marked inside the black circle. This shows that the population A is created mostly by the electrons that are pushed in front of the pulse. All the electrons that are outside the circle belong to the population B. They are plotted either as a black unaccelerated dots on the sides of the pulse or they are already starting to form lines perpendicular to the laser propagation direction by being attracted to the center of the beam with a high intensity laser field.

In Fig. 11(c), the population B is already accelerated and is located inside the target. The blue line showing the critical density

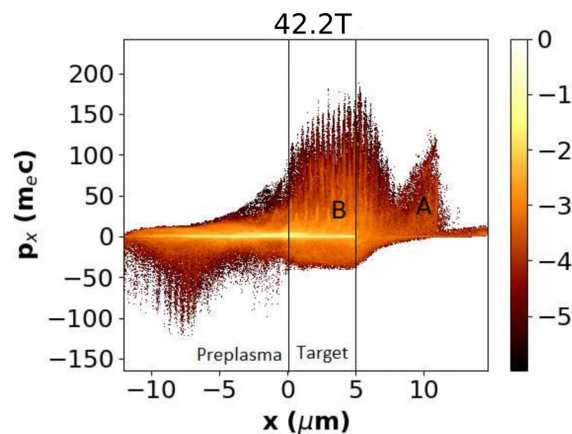


FIG. 10. The phase space of the electrons after the incidence of the laser pulse with the intensity of 10^{21} W/cm^2 on the target with preplasma. Color shows the relative amount of electrons where numbers on the color bar correspond to the exponent on the logarithmic scale.

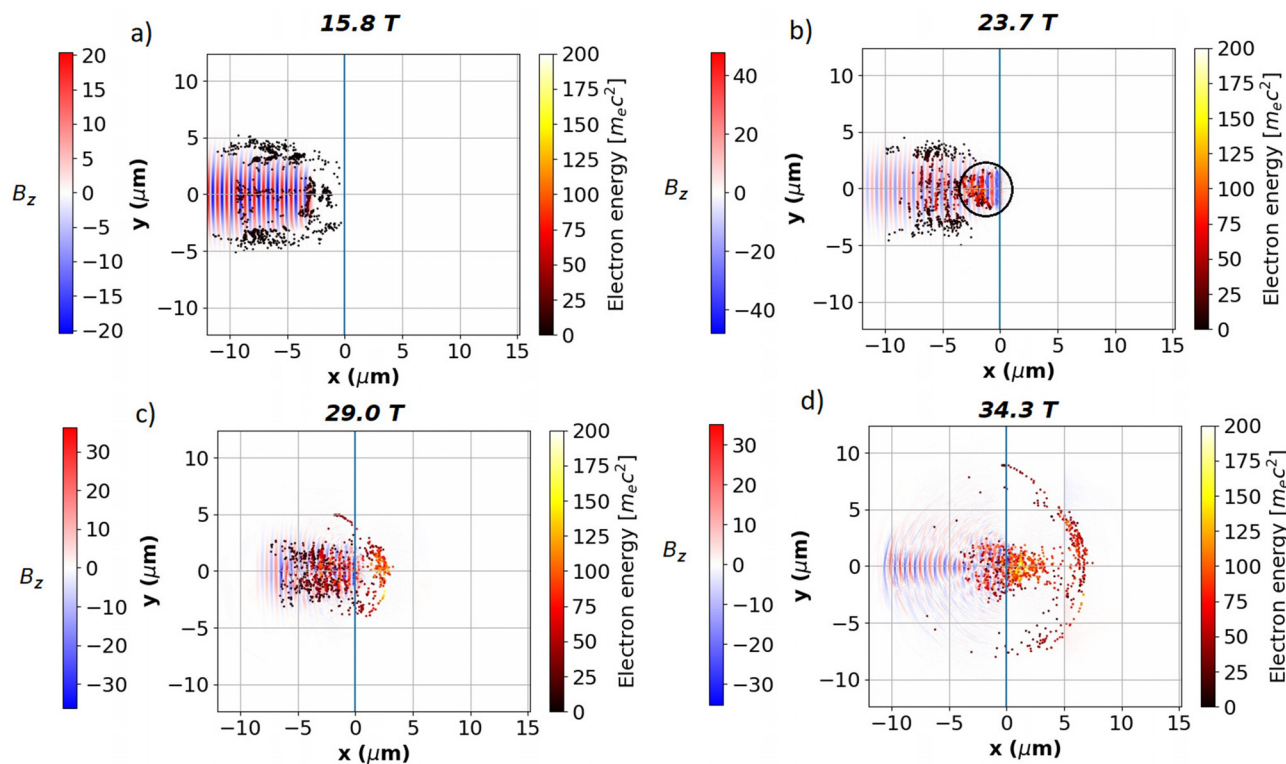


FIG. 11. Positions and energies of hot electrons during the acceleration by the laser pulse with the intensity of 10^{21} W/cm^2 on the target with preplasma. (a) Traveling wave repels electrons; (b) electrons are injected into the pulse at the positions where the standing wave was already created. Electrons from the population A are marked by the black circle. Electrons outside the circle belong to population B. (c) and (d) Electrons are accelerated in the field of the standing wave.

28 August 2023 08:54:17

layer roughly separates the population A from the population B. All the electrons that were previously on the sides of the laser pulse were attracted to the high intensity region of the pulse and they are accelerated toward the overdense part of the target.

In Fig. 11(d), most of the electrons from the first population already crossed the rear side of the foil and the majority of electrons

from population B is propagating inside the target while the small part still interacts with the standing wave in front of the target.

Two populations (A and B) are also easily observed in Fig. 12 where the initial positions and times of the start of the acceleration are shown. The initial time of the acceleration is again defined as a time when p_x has a minimum value. The black arrow represents the position of the front of the laser pulse. The point $(23.5T, 0 \lambda)$ represents the time when the constant part of the laser pulse is reflected from the overdense plasma. The arrow coming from this point separates two hot electron populations from each other. On the left, straight lines parallel to the incident wave's front correspond to the times when the electrons were pushed by the propagating laser pulse toward the target. Electrons depicted on the right were not pushed by the propagating beam. Instead, they were injected into the high-intensity part of the laser pulse from the sides and afterwards they were accelerated similarly to the case describing pulse with intensity 10^{18} W/cm^2 . Again, the maximum distance of the acceleration at a certain time is constrained by the position of the reflected wave's front. For those electrons, the standing wave seems to be in an inevitable condition for the acceleration to occur.

After a look on the y position of a typically accelerated electron from the population B in Fig. 13(b), it can be seen that the electron was moving toward the center of the laser pulse before it was accelerated. This electron movement along the target surface to the center of the laser pulse is caused by the p_y momentum component oscillating

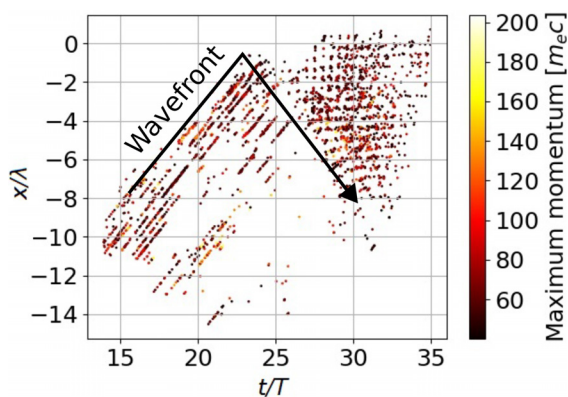


FIG. 12. Times and positions when the electron acceleration toward the target started during the interaction with normally incident pulse of intensity 10^{21} W/cm^2 on the target with preplasma. Black line shows the position of the laser wave's front before and after the reflection from the overdense plasma layer.

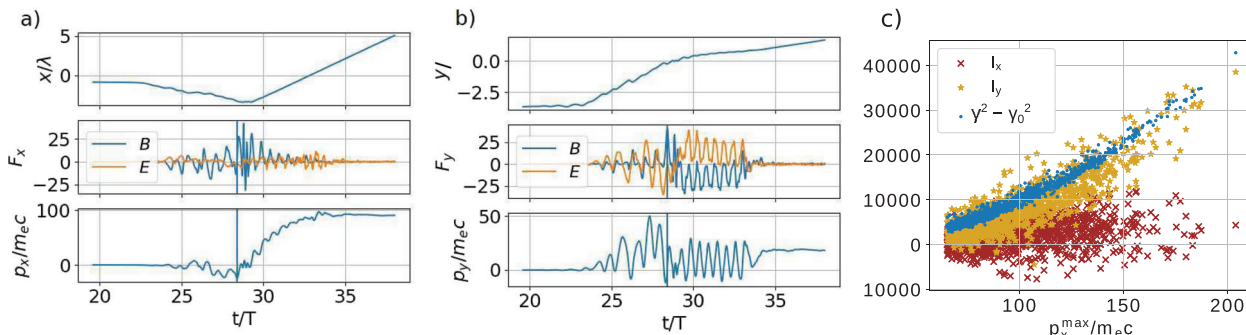


FIG. 13. Evolution of the forces acting on the electron during its acceleration, position, and momentum of the electron when the laser pulse with the intensity of 10^{21} W/cm^2 is incident on the target with preplasma. Vertical line indicates the moment of acceleration according to our definition. (a) x components; (b) y components; and (c) the contribution of the electric field components at the time of p_x maximum and the increase in gamma factor.

in positive values before the blue vertical line showing the starting time of the acceleration used in Fig. 12. Such injection into the high-field regions occurs because of the standing wave and plasma channel field and is further analyzed in Sec. V. After the electron injection into the high field region, it is accelerated toward the target, see Fig. 13(a) where the electron was consecutively accelerated during five laser periods while it propagated toward the overdense target in the standing wave. Additive impact of several pushes from the standing wave while it propagated in the preplasma allowed the electron population to be heated to temperature close to the ponderomotive scaling⁸ $T_h = ((1 + a_0^2)^{1/2} - 1)m_e c^2$, where T_h is the hot electron temperature in eV. Namely, the temperature of hot electrons observed in the simulation was 8.3 MeV, using Boltzmann distribution. Temperatures of hot electrons were higher than those predicted by the Beg's scaling.⁶ For the case of lower intensity, hot electron temperatures even exceed the ponderomotive scaling. The temperature of hot electrons accelerated in the target with the preplasma exceeds the temperature of electrons accelerated by the pulse with same intensity in the target with steep density gradient. This was observed for both laser intensities, see Table I.

To determine the acceleration mechanism, we calculated the contribution of electric field components to the acceleration and compared the values at the moment of p_x maximum, see Fig. 13(c). The integral I_x corresponds to the contribution of longitudinal electric field. It is usually not significantly present during the normal incidence. However, the radiation pressure deformed the overdense target surface into the parabolic-like shape which focused the laser pulse and turned the E_y component of the laser field into the x -direction. The relativistic self-focusing and charge separation are also present but it is not

possible to distinguish between the possible E_x field sources because of the simulation complexity. The integral I_y corresponds to the contribution of the standing wave and the background transverse field. Since the difference between the electron temperatures for different linear polarization geometries was previously observed,³⁴ we performed simulations of the target with preplasma also with s-polarized pulse. They showed that the interaction with p-polarized pulse leads to higher electron temperatures. We propose the following explanation: when electrons are accelerated by the standing wave, they oscillate in either positive or negative values of p_y [see Fig. 13(b)] while the magnetic field of the standing wave transfers the momentum into the x -direction. When the background field of plasma channel is present, the channel electric field can increase the mean value of p_y oscillations. Therefore, the higher transverse momentum can be transferred into the x -direction by the standing wave's magnetic field which results in higher electron momentum and temperature. When oscillating electric field is oriented out of the simulation plane in s-polarized pulse, the effect of the background electric field on electron energy is not present and results in lower electron temperatures. The positive value of Lyapunov exponent obtained from electron trajectories indicates that the mechanism of electron acceleration corresponding to I_y is stochastic heating.

The effect of the longitudinal electric field and stochastic heating on the electron acceleration is comparable for electrons with lower maximum momenta ($p_x^{\max} < 120 m_e c$). On the other hand, stochastic heating is the dominant acceleration mechanism for the most energetic electrons. Typical electron trajectories are depicted in Fig. 14. At the beginning, electrons are located on the sides of the laser pulse because they were repelled by the ponderomotive force. After some time, they are injected into the beam center where they are accelerated by the mechanisms described above. The injection mechanism is explained in Sec. V.

The influence of the preplasma scale length on electron energies was examined by two additional simulations with p-polarized pulse. Shorter preplasma had a scale length $L_s = 2\lambda$ ($1.6 \mu\text{m}$) and longer preplasma scale length was set to $L_s = 6.25\lambda$ ($5.0 \mu\text{m}$). The trend was apparent—longer preplasma resulted in higher electron energies. Maximum p_x for the shortest preplasma was $\approx 150 m_e c$, maximum p_x for moderate preplasma ($3.0 \mu\text{m}$) was $\approx 200 m_e c$, and the longest preplasma target resulted in electrons with almost $300 m_e c$.

TABLE I. Comparison of hot electron temperatures for different scenarios fitted using Boltzmann distribution compared with the ponderomotive scaling $T_{pond} = ((1 + a_0^2)^{1/2} - 1)m_e c^2$.

	T (keV)	T (keV)	T (keV)	T_{pond} (keV)
I (Wcm ⁻²)	steep density p-polarization	preplasma p-polarization	preplasma s-polarization	
10^{18}	24	250	150	96
10^{21}	4800	8300	7200	10 538

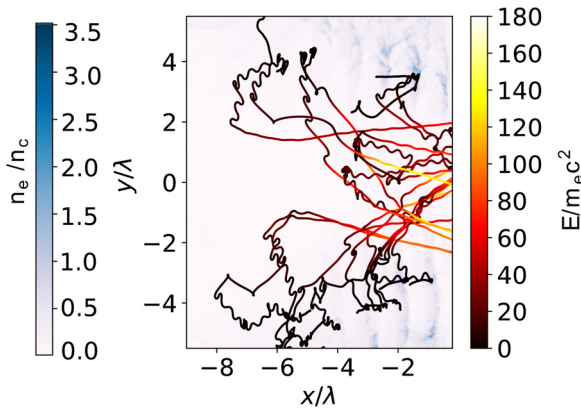


FIG. 14. Typical electron trajectories during their acceleration after the incidence of the pulse with intensity 10^{21} W/cm^2 on the target with preplasma. The repulsion of electrons on the sides of laser pulse can be observed from electron densities. Electrons oscillate on the sides of laser pulse (black part of trajectory) and they are injected into the beam axis region where the acceleration happens afterwards (red/yellow part of trajectory).

Higher electron energies in the case of moderate preplasma were the result of longer interaction length of electrons with the standing wave. The longer interaction length resulting in higher electron energies is a known property of stochastic heating.¹⁹ In the case of moderate preplasma, the maximum possible distance of interaction with the standing wave was already achieved (defined by the length of the laser pulse). This means that longer preplasma should not lead to higher energies if the stochastic heating is the only mechanism of acceleration present. The additional acceleration mechanism was observed for the case with the longest examined preplasma. When the laser pulse propagated in the preplasma, the modulation of laser pulse amplitude started to be developed, which created the lower amplitude region in the center. Electrons were captured inside this region in the center of propagating laser pulse (acceleration at the front of laser pulse was still present) and they were pre-accelerated even before the laser reflection. The pre-acceleration of electrons before the stochastic heating led to the higher electron energies. Similar phenomena were observed in Ref. 18. It caused the higher energies of accelerated electrons even

though the capturing mechanism is assigned to different effect in the reference.

An interesting property of p_x evolution for the majority of hot electrons was the negative momentum gain just before the acceleration into the target. This was however the same feature of all electrons being accelerated in four distinct interaction regimes described in this paper.

V. STANDING WAVE ELECTRON INJECTION

Ponderomotive force is well known for repelling particles from high field regions of the laser pulses down the gradient. However, the nature of the ponderomotive force in the standing wave changes. It was previously shown³⁵ that ponderomotive force by the standing wave in the relativistic regime can cause high-field regions to attract electrons. It was also shown that particles inside the standing wave exhibit complicated chaotic oscillations in Refs. 36–38. It can be seen in Fig. 11(b) that only electrons at the positions where the standing wave was already present (marked by black circle) were injected into the beam axis. Most of the electrons outside the circle are still on the sides of the beam, repelled by the incident pulse.

To closer investigate the injection mechanism in the standing wave into its high-field regions, we performed time-averaging of electromagnetic fields over one laser period as shown in Figs. 15(b) and 15(c). The region of non-zero averaged field can be observed in front of the target. Close to the beam axis, the field created due to the frequency shift of the reflected pulse is present. The overdense plasma surface is pushed by the ponderomotive pressure which causes the redshift of the reflected wave. This can be seen in the Fourier transform of the standing wave. In Fig. 15(a), $\omega_0 = 1$ corresponds to the incident wave frequency and peak on the left with slightly lower frequency equal to $\omega_R = 0.9$ is the frequency of the reflected wave. This creates $\approx \lambda/2$ wide regions of a non-zero averaged field with the periodic change of the sign.

Further from the beam axis ($|y| > 2\lambda$), the channel field^{39,40} dominates. It is created by the charge separation and acts on the repelled electrons in the direction toward the beam center. The channel field is also present close to the beam axis and the resulting time-averaged field is a superposition of the channel field and the field created by the red-shifted reflected and incident pulse.

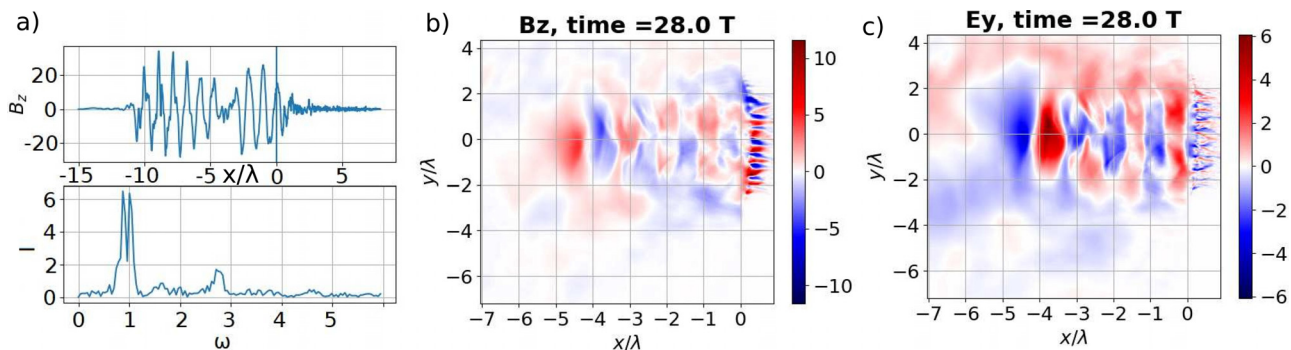


FIG. 15. (a) The magnetic field component of the standing wave for the pulse with the intensity of 10^{21} W/cm^2 at $y = 1.5\lambda$ and its Fourier transform. $\omega = 1$ corresponds to the incident wave and shifted peak of $\omega = 0.9$ corresponds to the reflected wave. (b) Magnetic field in front of the overdense target averaged over single laser period in times between 27 and 28 T. (c) The electric field in front of the overdense target averaged over the same laser period.

In order to examine the influence of the standing wave on the electron dynamics, we performed the simulation only with test particles interacting with two counter-propagating laser pulses with the intensity of 10^{21} W/cm^2 and identical temporal and spatial profiles like in the previous PIC simulations. Such an approach allows us to observe particle dynamics without the effects of collective plasma behavior on electron dynamics. The test particles were evenly spread across the simulation box and laser pulses crossed at $x = 0\lambda$ at time $t = 15T$. As can be seen in Fig. 16(a), the ponderomotive force pushes electrons in front of laser pulses and on the sides while the pulses propagate toward each other, in agreement with our PIC simulations of the pulse interacting with the preplasma. The vertical column of particles around the blue line represents the region between two counter-propagating pulses. Electrons in this region were either pushed by the pulses or they were initially placed there. Those electrons are also the source of electron population A in Sec. IV B. Figure 16(b) shows the position of electrons after the beams crossed. The front of the laser pulse propagating from the right is located approximately at $x = -5\lambda$, and the front of the pulse propagating from the left is located approximately at $x = 5\lambda$. The region where particles are present coincides with the area where the standing wave was already created due to the overlap of both pulses. This means that pushing electrons down the wave packet gradient is not the dominant ponderomotive force behavior and the particles are allowed to oscillate inside the high-intensity region in the standing wave at such intensities. At later times when pulses propagate further, the region where particles are not repelled increases. This clearly demonstrates that the creation of the standing wave by the reflected laser pulse had a strong impact on the injection of electrons into the standing wave in the case of laser pulse with the intensity of 10^{21} W/cm^2 incident on the target with preplasma.

The observation of electron trajectories in the phase space shows that the standing EM wave allows electrons to oscillate in the high-field regions instead of being repelled by the ponderomotive force. In general, trajectories vary greatly. However, several patterns can be observed, see Fig. 17. For example, Figs. 17(a)–17(d) correspond to the cases when electrons interact with the pulses of the same frequency and Figs. 17(e) and 17(f) show the electron dynamics in the field of

laser pulses with shifted frequencies. In Fig. 17(a), the $x - p_x$ trajectory oscillates around the position of B_z field antinode and the node of E_y field of the standing wave. In the $y - p_y$ trajectory, oscillation in positive p_y values is visible while the electron moves in the direction toward the beam axis at $y = 0$. This is in agreement with trajectories obtained from our PIC simulation with the laser pulse of intensity 10^{21} W/cm^2 , see Fig. 13. In Fig. 17(b), it can be seen how the electron skips from one B_z antinode to another in $x - p_x$ phase space. In $y - p_y$, the electron oscillates in negative p_y values and moves at first in the direction toward the beam axis and after it continues oscillating toward lower pulse intensity regions. In Fig. 17(c), the electron at first oscillates around the B_z antinode in the x -direction and afterwards it is accelerated to momenta exceeding values of oscillation in the laser field. The p_y momentum oscillates in the positive values and after some time starts to oscillate in negative values. The moment when the oscillation sign changes is identical to the time when the electron starts to be accelerated in the x -direction. In Fig. 17(d), the immediate acceleration by the standing wave to high energies without the oscillation around the E_y node is present.

The case in Figs. 17(e) and 17(f) demonstrates the impact of reflected wave's shifted frequency. The frequency of the pulse propagating from the left was set to $0.9\omega_0$, where ω_0 is the frequency of the pulse propagating from the right boundary. The shift of oscillation center in the x -direction is the only observed difference compared to the situation when the pulses with identical frequencies counter-propagate.

The discussion above allows us to describe the electron injection in the following way: at first, electrons are repelled by the propagating laser pulse far from the laser beam axis. The channel field pushing the electrons toward the beam center is simultaneously created. However, the ponderomotive force overcomes the effect of the channel background field and keeps the electrons on the sides of the laser pulse. After the reflection of an incident laser wave, the standing wave starts to be created and electrons are no longer repelled by the ponderomotive force. Instead, they oscillate around the magnetic field antinodes. This allows electrons to be injected by the channel field closer to the beam axis where the motion is dominated by the standing wave. There, electrons are either accelerated in the x -direction or they

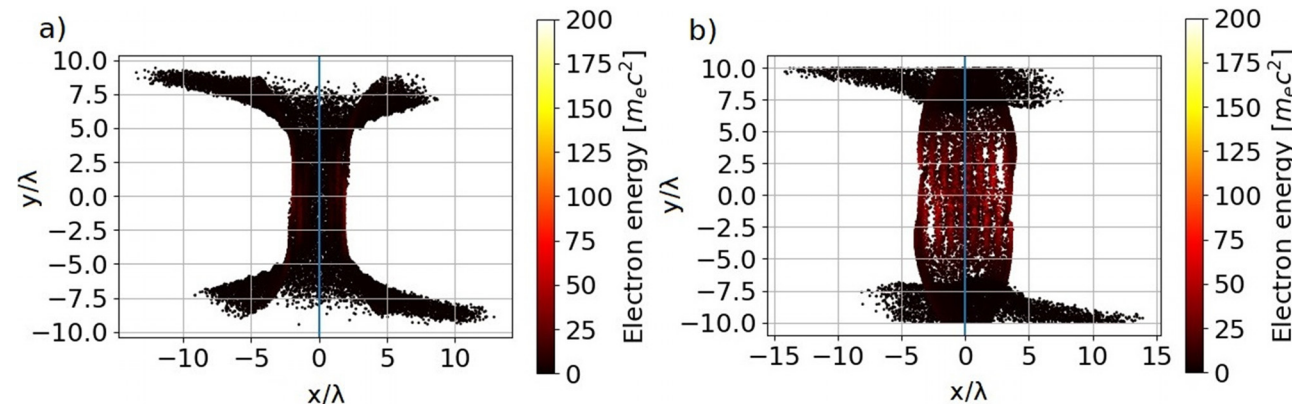


FIG. 16. (a) Positions of electrons at the time instant when laser pulses of intensity 10^{21} W/cm^2 were propagating toward each other. Test electrons are repelled by the ponderomotive force from the region where pulses are located. (b) Positions of electrons after laser pulses overlapped and created a standing wave present at $x = [-5, 5]\lambda$. Electrons are no longer repelled from the high-field regions and oscillate inside the standing wave.

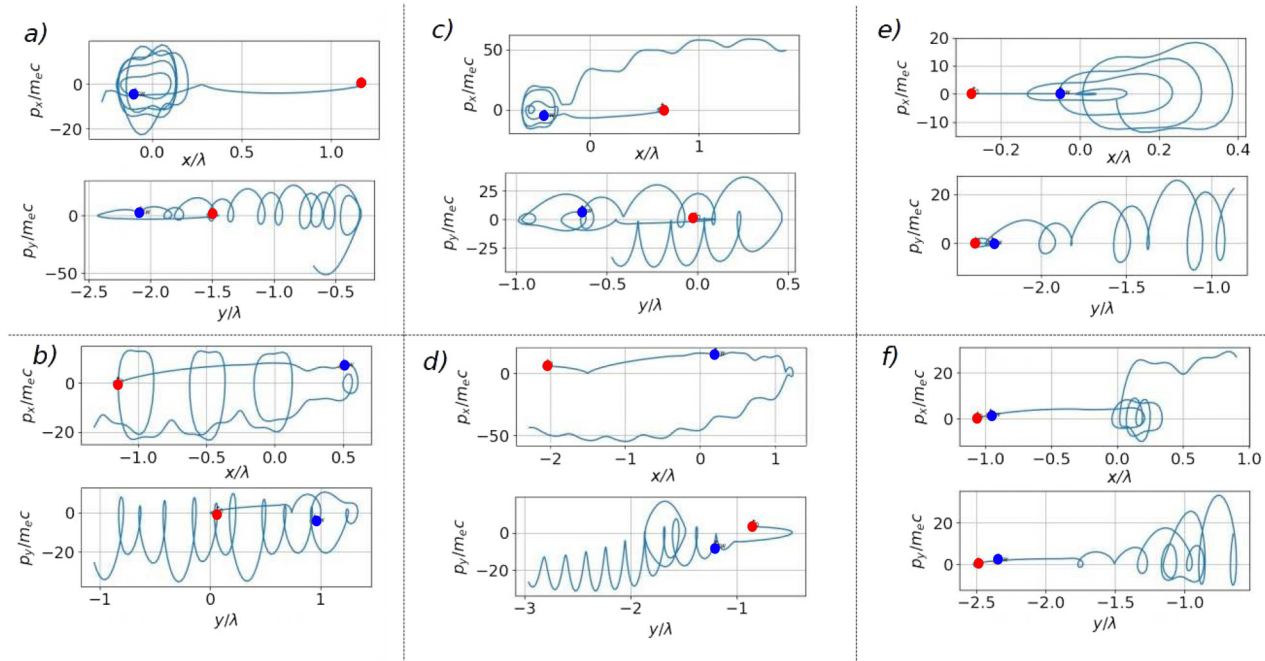


FIG. 17. Example phase space trajectories of the electrons in the field of the standing EM wave. Red dots correspond to the initial time of the simulation and the blue dots correspond to the time $15T$ when pulses started to overlap. (a)–(d) were obtained for counter-propagating pulses with identical frequencies, (e) and (f) for the pulses with shifted frequencies.

oscillate around the B field antinode while they are injected further in the transverse direction.

VI. CONCLUSION

We have demonstrated that hot electron acceleration mechanisms strongly differ depending on the laser intensity and density profile. For the case of 10^{18} W/cm^2 intensity and the steep plasma gradient, we showed that electrons are ejected into the vacuum by the electrostatic field where they interact with the standing wave. They start to be accelerated back into the plasma at times, when magnetic field changes its polarity, which happens twice in a laser period. The increase in the intensity to 10^{21} W/cm^2 caused the deformation of the overdense plasma boundary, which resulted in chaotic oscillations of electrons before the acceleration. Without the presence of preplasma, electrons were accelerated at the vacuum-plasma boundary by the $\vec{j} \times \vec{B}$ heating.

The presence of preplasma caused, that all electrons were accelerated in the underdense region, which resulted in significantly higher hot electron temperatures. According to our simulations, the p-polarized laser pulse leads to higher electron temperatures compared to the simulations with s-polarized pulse. We proposed an explanation based on the impact of background plasma channel field on the electron dynamics in the field of the standing wave. For the intensity of 10^{18} W/cm^2 , the irreversible energy gain was not present until the moment, when the reflected laser wave reached the position of an electron. Afterwards, electrons were accelerated toward the overdense part of the target. The stochastic acceleration mechanism was responsible

for the acceleration along with the longitudinal electric field present in the preplasma. When the laser pulse with the intensity of 10^{21} W/cm^2 was incident on the target, two distinct electron populations can be distinguished. The first population of hot electrons was pre-accelerated by the front of the laser pulse. The second population of hot electrons was initially repelled from the high-field regions by the ponderomotive force of the incident laser pulse. However, when the standing wave was created, they were injected back into the beam axis region along the magnetic field antinode and accelerated afterwards. This injection is a result of relativistic electron dynamics in the field of standing electromagnetic wave with the combination of the background plasma channel field. It was also demonstrated that a longer preplasma scale length results in higher electron energies.

ACKNOWLEDGMENTS

This work was partially supported by the CTU Project “Research on optical (nano)structures and laser plasma” No. SGS19/192/OHK4/3T/14.

Computational resources were supplied by the Project “e-Infrastruktura CZ” (e-INFRA LM2018140) provided within the program Projects of Large Research, Development, and Innovations Infrastructures.

J.P. also acknowledges the support and computational resources obtained from the European Regional Development Fund-Project CAAS (“Center of Advanced Applied Sciences”) No. CZ.02.1.01/0.0/0.0/16 _ 019/0000778.

³⁷G. Lehmann and K. H. Spatschek, "Phase-space contraction and attractors for ultrarelativistic electrons," *Phys. Rev. E* **85**, 056412 (2012).

³⁸Z.-M. Sheng, K. Mima, Y. Sentoku, M. S. Jovanović, T. Taguchi, J. Zhang, and J. Meyer-ter Vehn, "Stochastic heating and acceleration of electrons in colliding laser fields in plasma," *Phys. Rev. Lett.* **88**, 055004 (2002).

³⁹V. Khudik, A. Arefiev, X. Zhang, and G. Shvets, "Universal scalings for laser acceleration of electrons in ion channels," *Phys. Plasmas* **23**, 103108 (2016).

⁴⁰M. Vranic, R. A. Fonseca, and L. O. Silva, "Extremely intense laser-based electron acceleration in a plasma channel," *Plasma Phys. Controlled Fusion* **60**, 034002 (2018).